Supplementary Information (SI) for Journal of Materials Chemistry A.
This journal is © The Royal Society of Chemistry 2026

# *Electronic Supplementary Information (ESI)*

## Off-Stoichiometry-driven Electronic Structure Modulation leads to High Thermoelectric Performance in *n*-type InSb: An Experimental Study with Theoretical Insights

Usharani Valaparla,[a] Subhajit Sau,[b] Manojkumar Moorthy,[c] Sinorul Haque,[d,e] Tanmoy Ghosh,[f] Amarnath R. Allu,[d,e] Subhradeep Chatterjee, [g] V. Kanchana,[b]* and Suresh Perumal[a] *

[a] *Laboratory for Energy and Advanced Devices (LEAD), Department of Materials Science and Metallurgical Engineering, Indian Institute of Technology, Hyderabad (IITH), Kandi, Sangareddy, 502285, Telangana, India.*

[b] *Department of Physics, Indian Institute of Technology Hyderabad (IITH), Kandi, Sangareddy, 502285, Telangana, India.*

[c] *Institut de Chimie et des Matériaux Paris-Est, ICMPE –CNRS–UPEC2-8, rue Henri Dunant 94320 THIAIS-France.*

[d] *CSIR-Central Glass and Ceramic Research Institute, 196, Raja S. C. Mullick Road, Kolkata 700 032, India.*

[e] *Academy of Scientific and Innovative Research (AcSIR), Ghaziabad 201002, India*

[f] *Department of Energy and Human Sciences, Rajiv Gandhi Institute of Petroleum Technology, Jais, Amethi, Uttar Pradesh 229304, India.*

[g] *Department of Materials Science and Metallurgical Engineering, Indian Institute of Technology, Hyderabad (IITH), Kandi, Sangareddy, 502285, Telangana, India.*

* *Corresponding author E-mail: kanchana@phy.iith.ac.in and suresh@msme.iith.ac.in*

**2. Experimental procedure:**

### 2.1. Material synthesis and densification:

High-quality polycrystalline ingots (~ 6g of which In: 2.9272 g and Sb: 3.0728 g) of $InSb_{1-x}$ (x = 0.00, 0.01, 0.02, 0.03, 0.06 and 0.09) were synthesized by weighing the stoichiometric ratios of puratronic (99.999 %) In and Sb shots procured from the Alfa-Aesar and subsequently sealed in a quartz tube of 10 mm diameter under vacuum of $\sim 1 \times 10^{-4}$ mbar and thereafter placed in a programmable muffle furnace. The sealed tubes with samples were heated to 923 K in 6 h, soaked for 6 h and subsequently cooled to room temperature over 10 h, resulting in cylindrical specimens with a diameter of 10 mm. The ingots removed from the quartz tube were pulverized into powder using an agate mortar and pestle. To measure thermoelectric properties, as-synthesized powders were compacted using a home-made induction-assisted hot press at a temperature of 723 K for a time duration of 10 minutes with the applied pressure of ~50 MPa under a vacuum atmosphere. The density of the sintered pellets was measured using Archimedes' principle, and all the samples were found to be above 92% of the theoretical density.

### 2.2 Material characterization

Powder X-ray Diffraction (P-XRD) data of all samples $InSb_{1-x}$ (x = 0.00, 0.01, 0.02, 0.03, 0.06 and 0.09) were acquired using a Bruker Rigaku Ultima-4 diffractometer with a Cu-$K_\alpha$ ($\lambda$ = 1.5406 Å) radiation. Raman vibrational studies were carried out on pellet samples using a WITech alfa300 R confocal Raman Spectroscopy by utilizing the 532 nm laser (Power, acquisition time) Optical bandgap studies of all samples were performed using diffuse reflectance spectroscopy (DRS) with Nicolet iS50 RaptIR Micro-FTIR Spectrometer in the wavenumber range of 4000–650 $cm^{-1}$, with a resolution of 4 and 32 scans. Further, the absorption coefficient ($\alpha/S$) was calculated using the Kubelka-Munk expression, $\alpha/S = (1-R)^2/(2R)$, where R is the reflectance, $\alpha$ and $S$ are absorption and scattering coefficients, respectively, and the optical bandgap ($E_g$) of all the samples was determined from the graphs plotted against $\alpha/S$ *vs.* energy (eV). The polished pellets' morphological and chemical analyses were examined using JEOL JIB 4700 F focused ion beam scanning electron microscopy (FE-SEM).

### 2.3 Thermoelectric measurements

The electrical conductivity (σ) and Seebeck coefficient (*S*) measurements of the rectangular bars with the dimensions of 8 × 2 × 2 mm³ were done simultaneously under a Helium atmosphere using a commercial ULVAC-RICO ZEM-3, thermoelectric measurement system. Hall measurement was done at room temperature in the homemade setup where a fixed magnetic field and DC current were used to be 2T and 0.2 mA, respectively. Thermal diffusivity (D) and specific heat capacity ($C_p$) of 2 mm thickness and 10 mm diameter samples were measured in the temperature range of 300 – 673 K using the laser flash diffusivity method on a NETZSCH LFA-467 system. The temperature-dependent heat capacity was derived using a standard sample (Pyroceram) in an LFA-467, which is in good agreement with the Dulong-Petit $C_p$ value. The total thermal conductivity ($\kappa_{total}$) of all samples was calculated using the formula $\kappa_{total} = D.C_p.\rho$, where ρ represents the measured density. The density (ρ) of all the pellets was measured by Archimedes' method, and the relative densities of pristine and Sb-deficient samples were around ~ 92% of the theoretical density. The nanoindentation experiment was performed for pristine InSb and $InSb_{0.99}$ pellets using a Nios scanning nano hardness tester with 5 s of loading and unloading time and 2 s of holding time with a load of 10 mN applied to the samples. The relation $H = P_{max}/A$, where $P_{max}$ and A represent the applied maximum load and area of contact at maximum load, respectively, is used to calculate the hardness of materials. Furthermore, a cyclic loading experiment with multiple loads was conducted on the samples, where the maximum load ranged from 1 to 10 mN, with each load being held for 1 s. The unloading amount was set at 50% of the maximum load, and the load cycle was repeated 100 times. The calculations of $ZT_{eng}$, $PF_{eng}$, $\eta_{TE}$, TE device figure of merit with the efficiency of uni-couple (a pair of single *p*- and *n*-type legs) are provided in the supporting Information, SI section.

### 2.4 Theoretical investigation

Density-functional theory (DFT), [1] calculations were performed and presented in this work using VASP code (version 5.4.4). [2,3] We used the projector-augmented waves (PAW) approach to represent valence and core electrons. The exchange and correlation function was treated with generalized gradient approximation (GGA) at the Perdew-Burke-Ernzerhof (PBE) level.[4] The valence electronic configurations included in the atomic pseudo-potentials for the calculations are In ($4d^{10}5s^25p^1$, version 6 Sep 2000), Sb ($5s^25p^3$, version 6 Sep 2000). The calculations were performed using the ‘‘accurate’’ precision setting. The plane wave energy cut off $E_{cut}$ was set at 500 eV, and energy convergence of electron relaxation at $10^{-6}$ eV. The force convergence is set

at $10^{-2}$ eV/Å for structural relaxation. Given the high computational cost associated with large supercells in optimization and phonon calculations, a 2 × 2 × 4 supercell (total 32 atoms i.e. 16 In and 16 Sb) of primitive unit cell (containing 2 atoms) of InSb was employed in the DFT simulations. Due to the limited supercell size, only the $InSb_{0.94}$ defect was considered. This defect model (x = 0.06) consists of 31 atoms (with 16 In and 15 Sb atoms). The density of states was calculated using the tetrahedron method with *k*-points of 8 × 8 × 4 for Brillouin zone integration for both pure and defect structures in the 2 × 2 × 4 supercell. In the calculations, we considered spin-orbit coupling. Next, the crystal overlap Hamilton population (COHP) analysis of the local bonding characteristics is performed via the LOBSTER code (v 5.0.0).[5] The phonon dispersions are obtained using the 2 × 2 × 4 primitive unit cell of pristine InSb using the Phonopy code.[6]

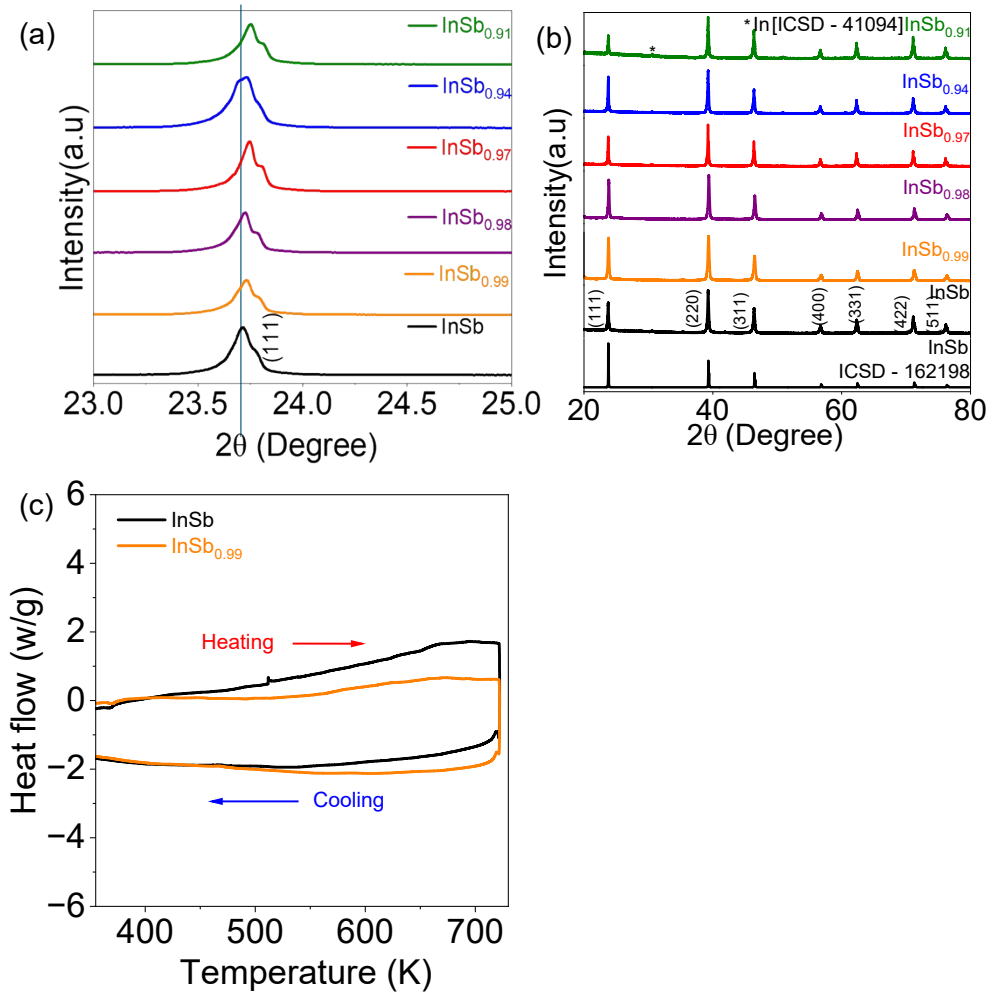


Fig. S1 (a) Zoomed XRD pattern of $InSb_{1-x}$ (x = 0.0, 0.01, 0.02, 0.03, 0.06 and 0.09) samples. (b). Pellet XRD pattern $InSb_{1-x}$, (c). DSC curves of pristine InSb and Sb-deficient $InSb_{0.99}$ samples.

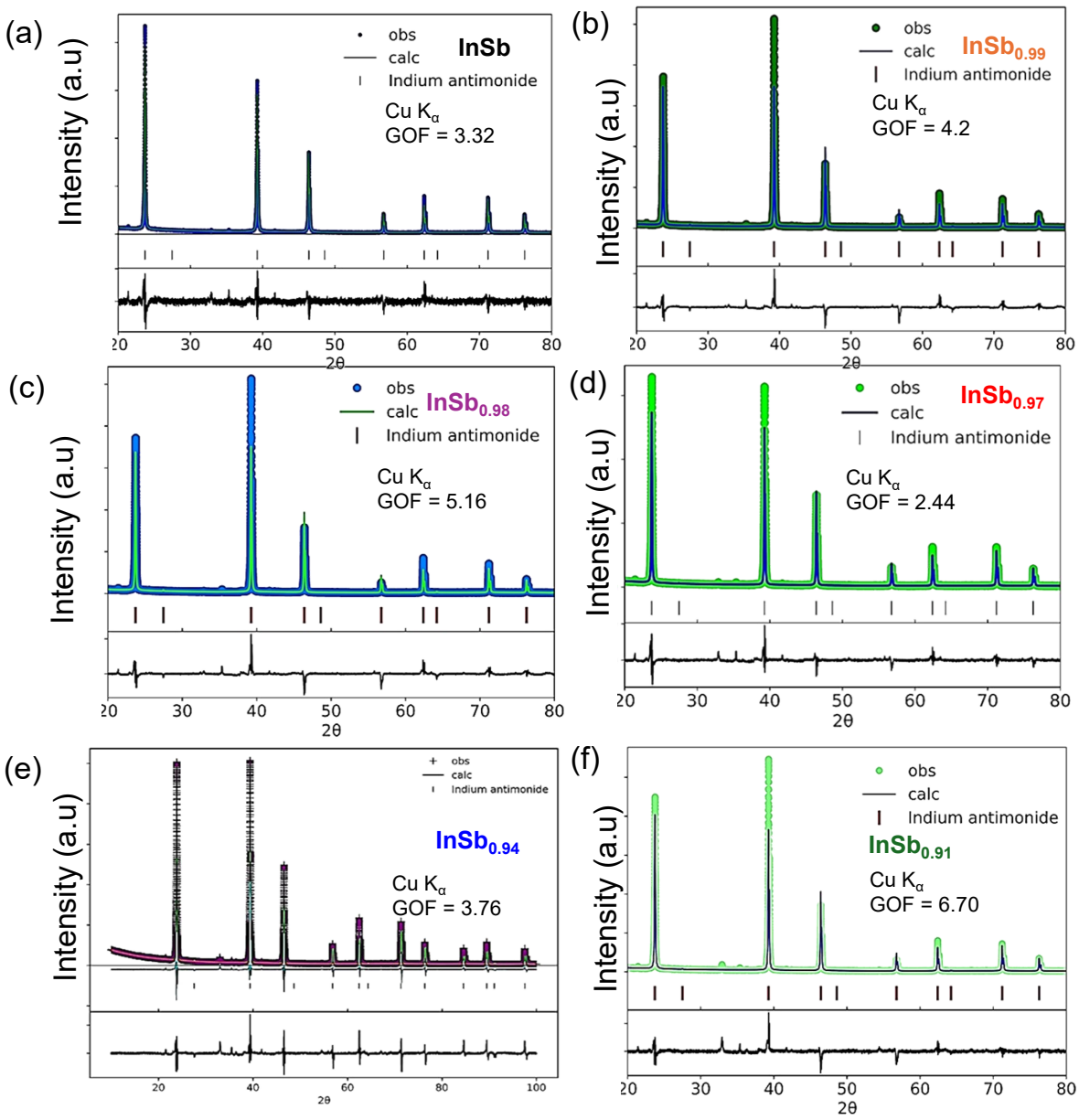


Fig. S2 (a) - (f) Refinement of $InSb_{1-x}$ (x = 0.0, 0.01, 0.02, 0.03, 0.06 and 0.09) samples. The Rietveld refinement of $InSb_{1-x}$ (x = 0.0, 0.01, 0.02, 0.03, 0.06 and 0.09) samples was done using GSAS-II software and displayed in a Fig. S2 (a) - (f). As antimony deficiency was increasing from x = 0.0 to x = 0.09, the lattice parameters $a = b = c$ and the volume ($V$) decreased, as displayed in Table S1.

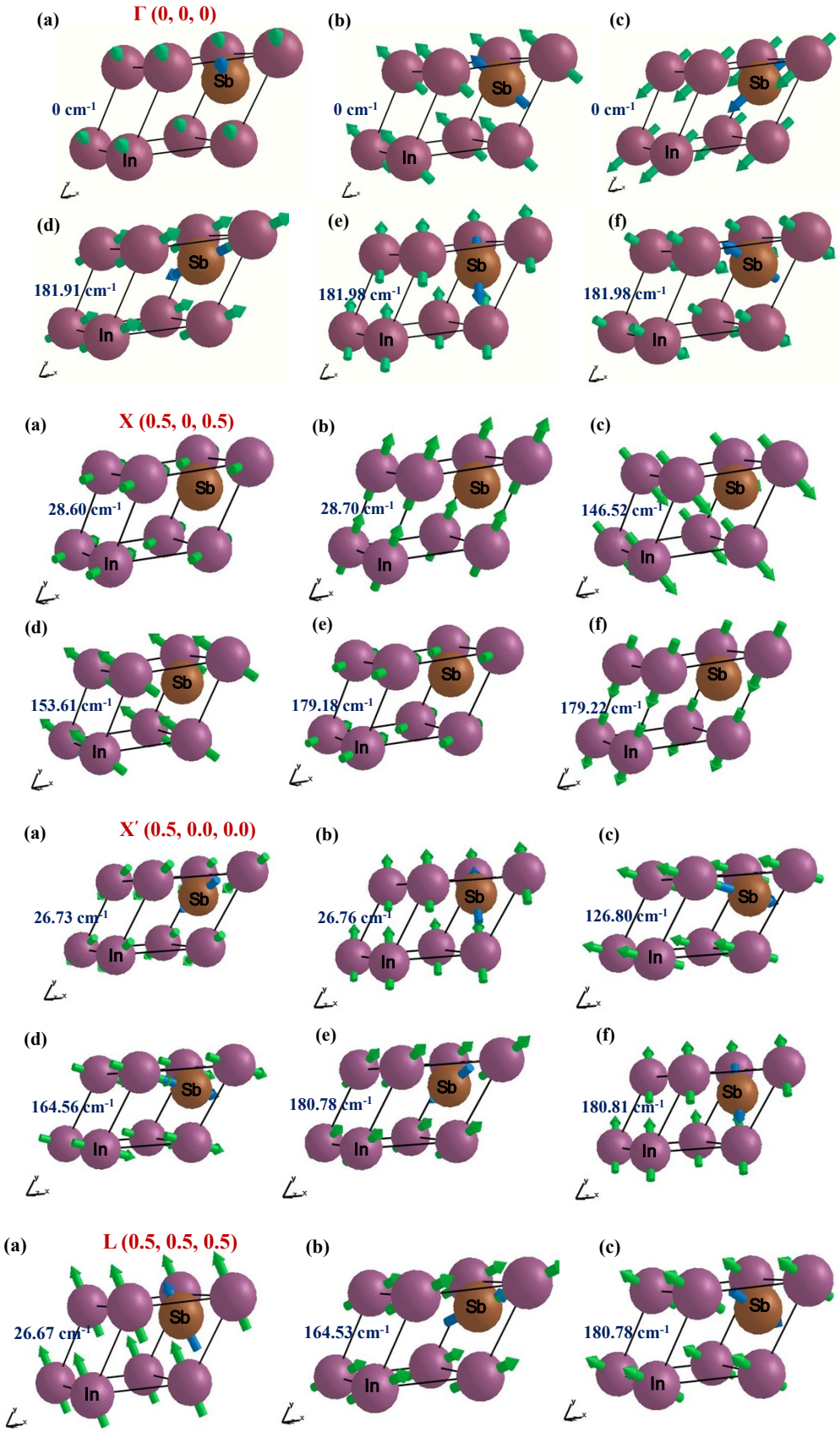


Fig. S3 (a) - (f) Raman-active vibrational modes of pristine InSb at high symmetry points of Γ (0,0,0), X(0.5,0,0.5), X'(0.5,0,0) and L(0.5,0.5,0.5).

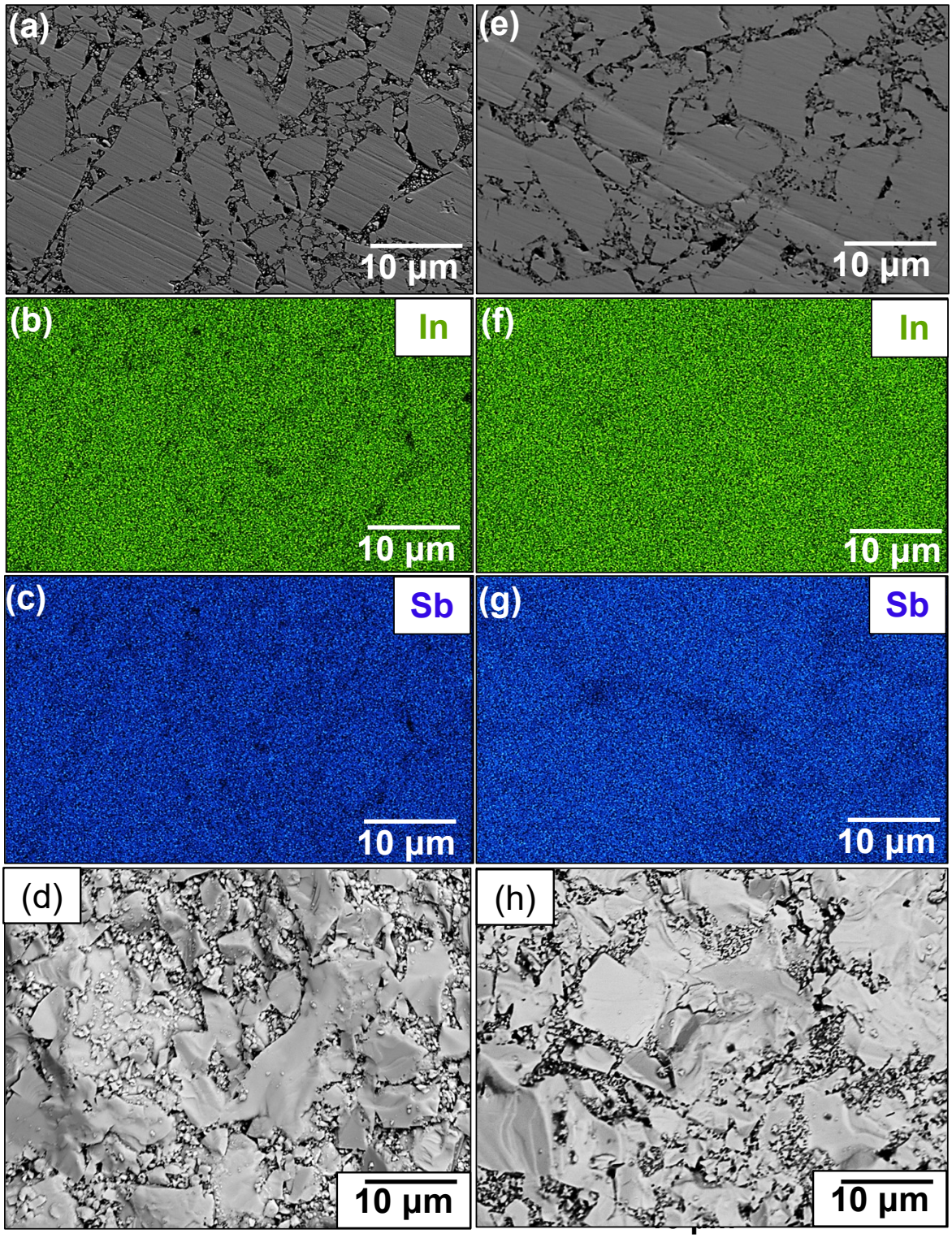


Fig. S4 (a) Back Scattered Electron (BSE) micrograph of polished surface of InSb (b) and (c) Elemental mapping of In and Sb (d) BSE fractured surface of InSb (e) BSE micrograph of polished $InSb_{0.91}$, (f) and (g) Elemental mapping of In, Sb, and (h) BSE fractured surface of $InSb_{0.99}$ samples, respectively.

Fig. S4 (a) and (b) represent the BSE micrographs of mirror-polished InSb and $InSb_{0.99}$ pellets, which illustrate the homogenous microstructures with no second phase in InSb, confirming the phase purity of InSb even after hot press. The compositional analyses *via* EDS elemental mapping were recorded for InSb and $InSb_{0.99}$, as seen in Fig. S4 (b) (g) which collectively depict the elemental compositions of 49.5 at.% for In and 50.5 at.% for Sb in InSb, and similarly, 50.4 at.% of In 47.6 at.% for Sb in $InSb_{0.99}$, confirming the existence of off-stoichiometry in $InS_{0.99}$ sample. Fig. S4 (d) and (h) represent the BSE-assisted fractured micrographs of InSb and $InSb_{0.99}$ samples, respectively, illustrating that the grains of sintered pellets are densely packed without many voids and with an average grain size range of 10-30 micrometres, verifying the measured density from the Archimedes' method.

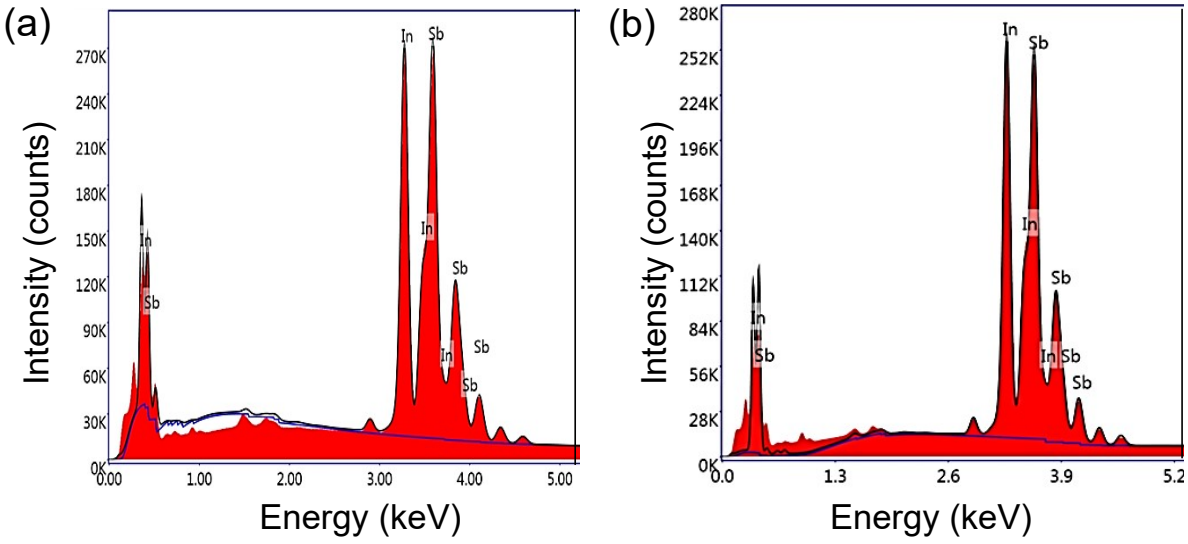


| Composition | In at.% | Sb at.% |
|---|---|---|
| InSb | 49.5 | 50.5 |
| $InSb_{0.99}$ | 52.4 | 47.6 |

Fig. S5 EDS and composition of (a) Pristine InSb. (b) $InSb_{0.99}$.

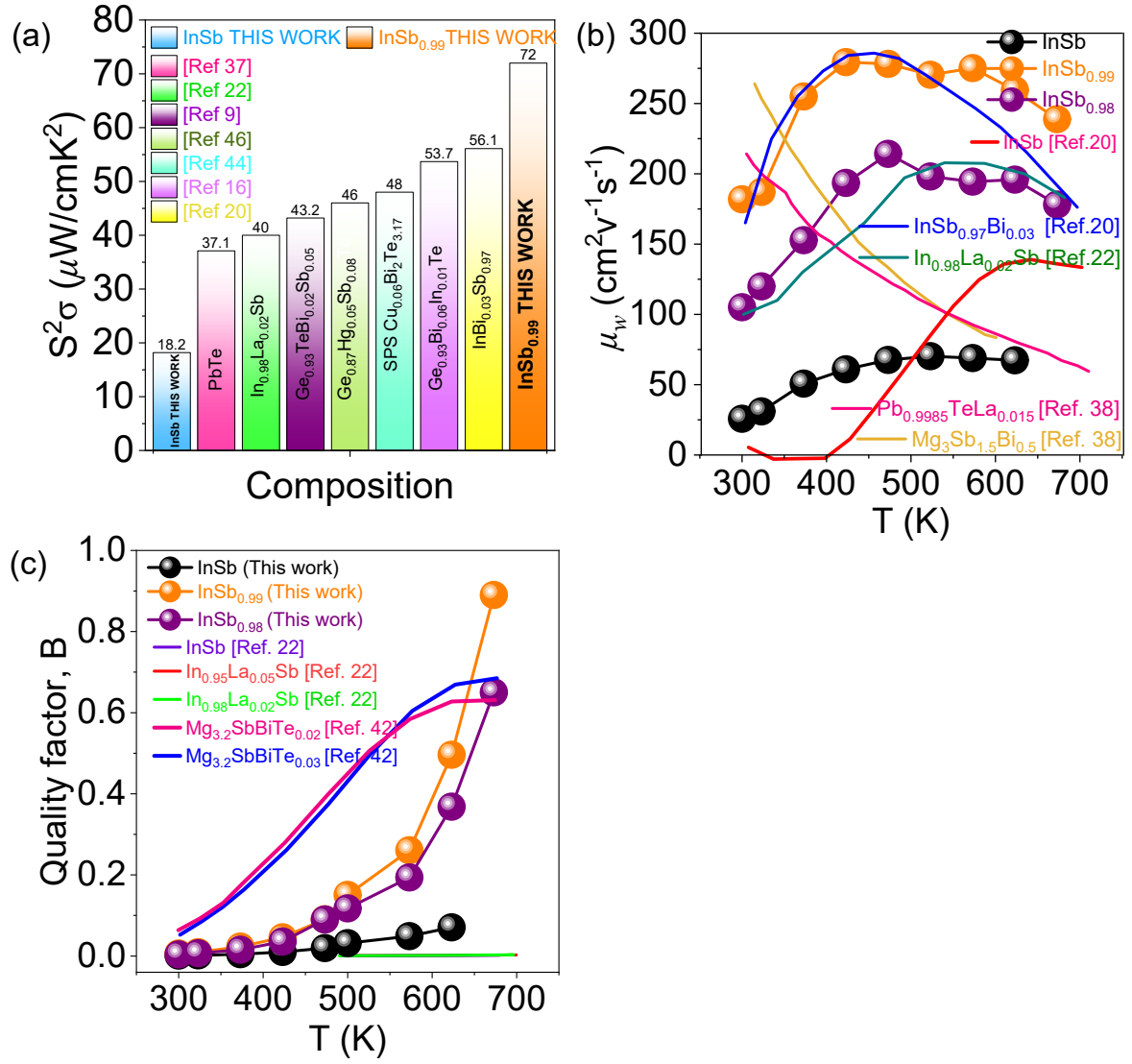


Fig. S6 (a) comparison plot InSb-based power factor with InSb thermoelectric material (b) comparison of Weighted mobility with other state-of-the-art materials. (c) Comparison plot InSb Quality factor, B, with state-of-the-art materials. (The above reference numbers are followed from the main manuscript references).

**Calculations of Weighted mobility and quality factor:**

The following equation was used to calculate weighted mobility ($\mu_w$) from the measured electrical conductivity (σ) and Seebeck coefficient (S): [7]

$$\mu_W = \frac{3h^3\sigma}{8\pi e(2m_e k_B T)^{3/2}}\left[\frac{exp[\frac{|S|}{\frac{k_B}{e}} - 2]}{1 + exp\left[-5(\frac{|S|}{\frac{k_B}{e}} - 1)\right]} + \frac{\frac{3\,|S|}{\frac{\pi^2 k_B}{e}}}{1 + exp\left[5(\frac{|S|}{\frac{k_B}{e}} - 1)\right]}\right] \quad (S1)$$

The following equations can be used to determine the transport coefficient and quality factor based on the electric conductivity, lattice thermal conductivity, and Seebeck coefficient measurements:

$$\sigma_E = \frac{\sigma}{\left(r + \frac{3}{2}\right) * F\left[r + \frac{1}{2}, \eta\right]} \quad (S2)$$

$$B = (\frac{k_B}{e})^2 * \frac{\sigma_E}{k_l} * T \quad (S3)$$

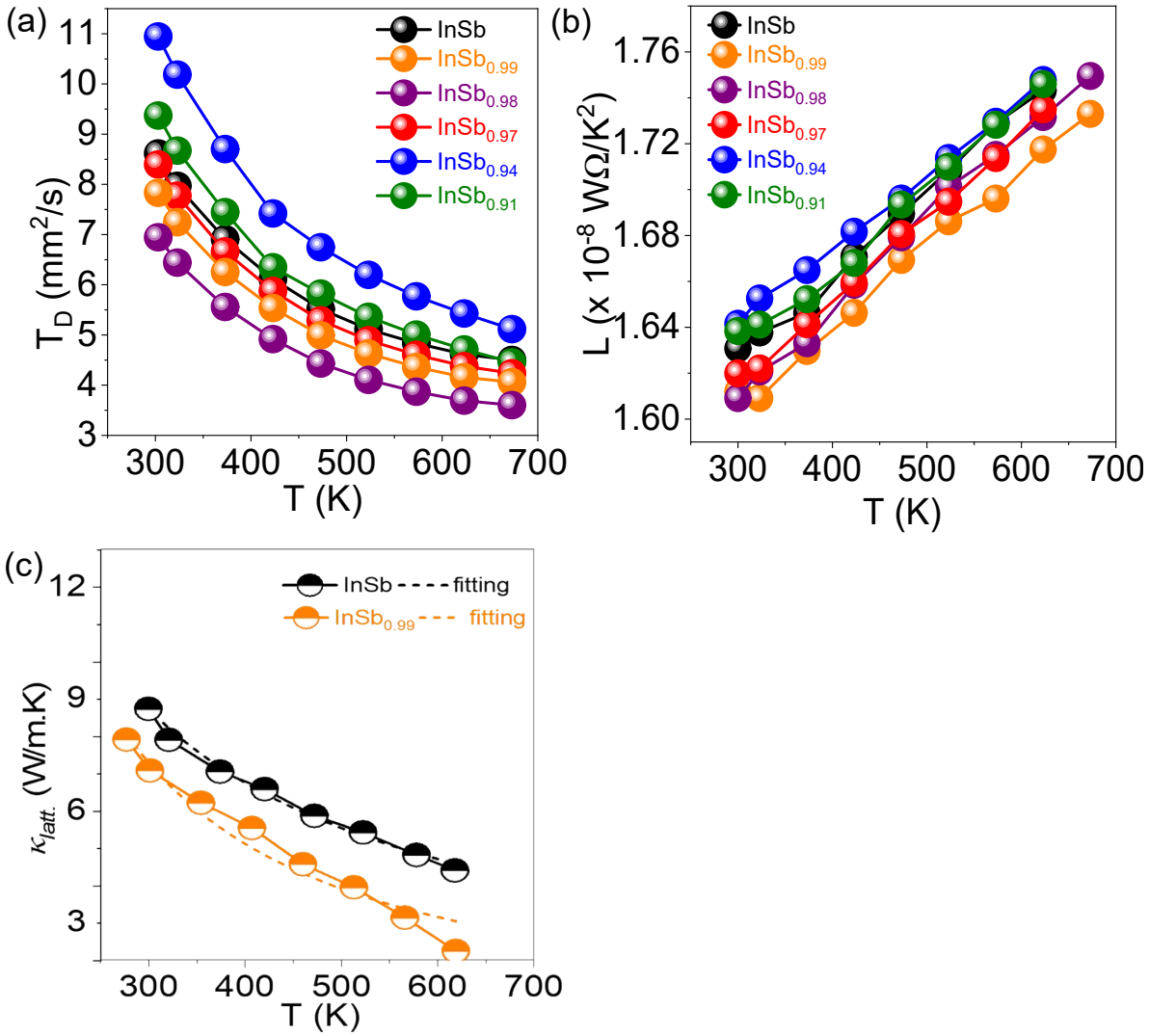


Fig. S7 (a) Thermal diffusivity, (b) Lorentz number of $InSb_{1-x}$ (x = 0.0, 0.01, 0.02, 0.03, 0.06 and 0.09) samples. (c) Lattice thermal conductivity ($\kappa_{latt.}$), where the dotted line shows the Debye-Callaway model fitting.

**Debye-Callaway Model:** To understand the off-stoichiometry-driven low thermal conductivity of $InSb_{0.99}$ and $InSb_{0.98}$ samples, we employed a Debye-Callaway model and fitted it to the $\kappa_{latt}$ *vs* T data using the following equation, which accounts for various scattering mechanisms.[8–10]

$$\kappa_{latt} = \frac{4\pi k_B^4 T^3}{\upsilon h^3} \int_0^{\theta_D/T} \tau \frac{z^4 exp(z)}{[\exp(z) - 1]^2} dz \qquad \text{(S4)}$$

Where $\theta_D$, υ, τ, and z stand for the Debye temperature, the mean sound speed, total phonon relaxation time, and the reduced phonon frequency, respectively. With the help of Matthiessen, the total relaxation time, τ can be written as,[9,10]

$$\tau^{-1} = {\tau_{PD}}^{-1} + {\tau_U}^{-1} + {\tau_N}^{-1} + {\tau_B}^{-1} + {\tau_D}^{-1} \quad \text{(S5)}$$

Here, ${\tau_{PD}}^{-1}$, ${\tau_U}^{-1}$, ${\tau_N}^{-1}$, ${\tau_B}^{-1}$, $and\ {\tau_D}^{-1}$ represent the scattering relaxation times of point defects, Umklapp-process, nano-inclusions, boundary, and dislocations, respectively. According to the Callaway model,[8] the grain boundary scattering can be ignored for the bulk and disordered crystals, especially the region T> $\theta_D$; so, the Umklapp (U) process and point defect scattering were considered in this study.

Thus, the total relaxation time for the Umklapp process and point defects is, [9,10]

$$\tau^{-1} = {\tau_{PD}}^{-1} + {\tau_U}^{-1} \quad \text{(S6)}$$

$$\tau_{PD}^{-1} = \frac{\gamma\omega^4}{4\pi\gamma^3}\Gamma \quad \text{(S7)}$$

$$\tau_{U}^{-1} = \frac{\hbar\gamma^2\omega^2 T}{\bar{M}\gamma^2\theta_D} e^{\frac{-\theta_D}{3T}} \quad \text{(S8)}$$

From equations (S5) and (S6), V, $\gamma$ , $\Gamma$ and $\bar{M}$ correspond to the average atomic volume, the Grüneisen parameter, the point defect scattering parameter and the average atomic mass, respectively. Therefore, equation (S6) can be rewritten into, [9,10]

$$\tau^{-1} = A\omega^4 + B\omega^2 T\, exp(-\frac{\theta_D}{3T}) \quad \text{(S9)}$$

Here, the parameters *A* and *B* belong to the point defects and the Umklapp process, which are given by,

$$A = \frac{V}{4\pi\gamma^3}\Gamma \quad \text{(S10)}$$

$$B = (1+\beta)\frac{\hbar^2\gamma}{\bar{M}\gamma^2\theta_D} \quad \text{(S11)}$$

Using the above relations, the Debye model was fitted to the $\kappa_{latt}$ vs T data of InSb and $InSb_{0.99}$ samples, which is illustrated by the fitted dashed lines in ESI, Fig. S7d, and then, extracted the *A* and *B* parameters, where $\theta_D$ and υ were used as ~168 K and 2300 $ms^{-1}$, respectively .[11]

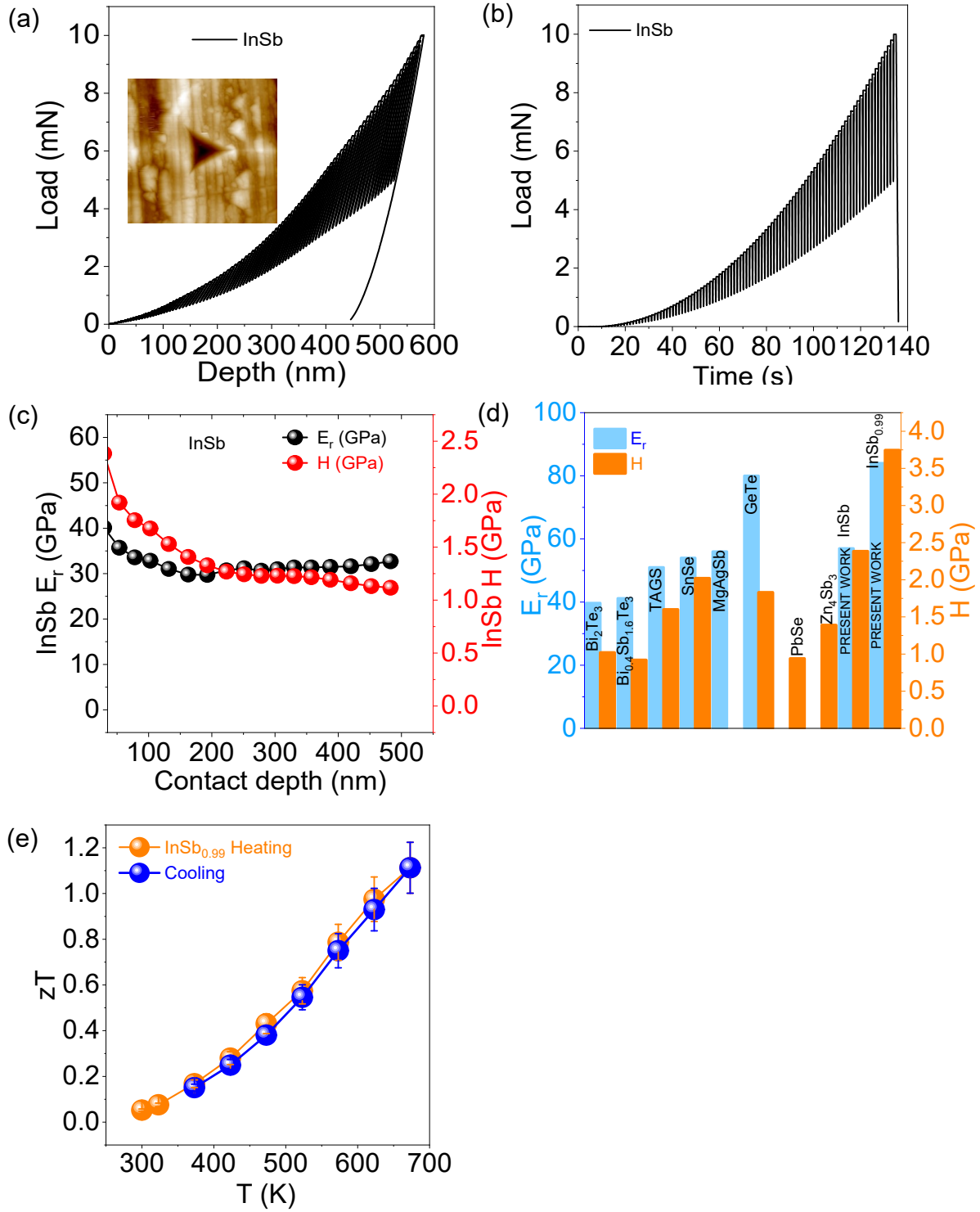


Fig. S8 (a) Load *vs.* Depth plot of pristine InSb (b) Load *vs.* Time plot of pristine InSb and (c) Er and H *vs.* contact depth of pristine InSb plot, (d) Comparison plot of Hardness and Young's modulus with other state-of-the-art TE materials (The plot (d) references are followed from the main manuscript reference [Ref.12] (e) zT plot of $InSb_{0.99}$ both heating and cooling.

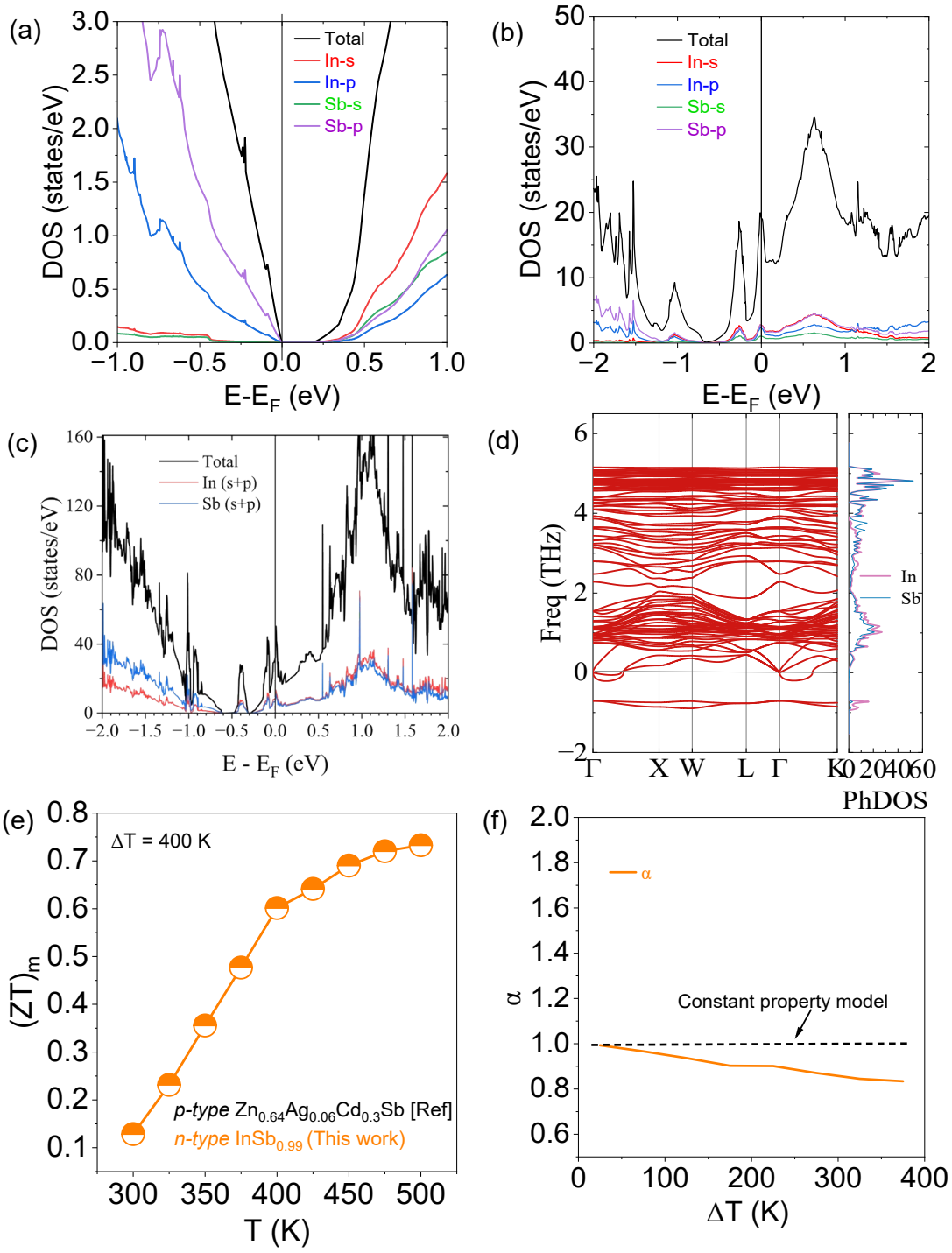


Fig. S9 DOS plot of (a) pristine InSb (b) $InSb_{0.94}$ calculated by without spin-orbit coupling (SOC). (c) DOS of $InSb_{0.99}$ (d) Phonon dispersion curve of InSb along high-symmetry path Γ(0,0,0)-X(0.5, 0.0, 0.5)-W(0.5, 0.25, 0.75)-L(0.5, 0.5, 0.5)-Γ(0,0,0)-K(0.375, 0.375, 0.75) of the Brillouin zone and (e) Theoretical device thermoelectric figure of merit $(ZT)_m$ for one pair of *n*-type (present $InSb_{0.99}$) and *p*-type (previously reported $Zn_{0.64}Ag_{0.06}Cd_{0.3}Sb$) legs as a function of temperature. (f) Computed dimensionless Thomson coefficient intensity factor (α).

## 1. Two-band model for the calculation of S *vs.* n data:

Within a single parabolic band model, the Seebeck coefficient (*S*), Hall carrier concentration ($n_H$), Hall carrier mobility ($\mu_H$), Hall factor (A) and electrical conductivity ($\sigma$) are given as [4,12]

$$S = \frac{k_B}{e}\left[\frac{2F_1(\eta)}{F_0(\eta)} - \eta\right], \qquad \text{(S12)}$$

$$n_H = \frac{(2m^* k_B T)^{3/2}}{3\pi^2\hbar^3} \cdot \frac{F_{1/2}(\eta)}{A}, \qquad \text{(S13)}$$

$$\mu_H = \mu_0 \frac{\sqrt{\pi}}{2} \cdot \frac{F_0(\eta)}{F_{1/2}(\eta)}, \qquad \text{(S14)}$$

$$A = \frac{3F_{1/2}F_{-1/2}}{4(F_0)^2}, \qquad \text{(S15)}$$

$$\sigma = n_H \mu_H e, \qquad \text{(S16)}$$

Where η is the reduced Fermi level, $k_B$ is the Boltzmann constant, and e is the electronic charge. The generalized Fermi integration is given by:

$$F_n(\eta) = \int_0^\infty \frac{\varepsilon^r}{1 + exp(\varepsilon - \eta)} d\epsilon \qquad \text{(S17)}$$

in which ε is the reduced energy. Then the Lorenz number is given by

$$L = \left(\frac{k_B}{e}\right)^2\left[\frac{3F_2(\eta)}{F_0(\eta)} - \left(\frac{2F_1(\eta)}{F_0(\eta)}\right)^2\right] \qquad \text{(S18)}$$

For a two-band model, the total electrical conductivity ($\sigma_{tot}$), Seebeck coefficient ($S_{tot}$), Lorentz number ($L_{tot}$), Hall coefficient ($R_{H,tot}$), Hall carrier concentration ($n_{H,tot}$) and carrier mobility ($\mu_{H,tot}$) are respectively given as:

$$\sigma_{tot} = \sigma_1 + \sigma_2 \qquad \text{(S19)}$$

$$S_{tot} = \frac{S_1\sigma_1 + S_2\sigma_2}{\sigma_1 + \sigma_2} \qquad \text{(S20)}$$

$$L_{\text{tot}} = \frac{L_1\sigma_1 + L_2\sigma_2}{\sigma_1 + \sigma_2} \quad \text{(S21)}$$

$$R_{H_{tot}} = \frac{R_{H_1}\sigma_1^2 + R_{H_2}\sigma_2^2}{(\sigma_1 + \sigma_2)^2} \quad \text{(S22)}$$

$$n_{H_{tot}} = \frac{1}{eR_{H_{tot}}} \quad \text{(S23)}$$

$$\mu_{H_{tot}} = \sigma_{\text{tot}} R_{H_{tot}} \quad \text{(S24)}$$

## 2. Calculations of $zT_{engg}$, PD, PF, and $\eta_{max}$ parameters

Generally, the thermoelectric figure of merit, zT, is strongly coupled with the interdependent parameters of S, σ and κ from which the TE efficiency will be calculated, wherein TE parameters are considered as temperature dependent. In a practical case, all the terms have a temperature dependency. So, H. S. Kim et al.,[13] have introduced the temperature-dependent terms as $ZT_{eng}$, $PF_{eng}$ and the corresponding efficiency, which governs the reliability in calculating the TE efficiency. Here, we have used the following equation for our calculations.

### a. Average figure of merit for a single-leg,

$$ZT_{avg} = \frac{\frac{S^2(T)}{\rho(T)} \times T}{\kappa(T)} \quad \text{(S25)}$$

### b. Engineering power factor,

$$PF_{eng} = \frac{\left(\int_{T_c}^{T_H} S(T)\,dT\right)^2 \Delta T}{\int_{T_c}^{T_H} \rho(T)\,dT} \quad \text{(S26)}$$

### c. Engineering figure of merit,

$$(zT)_{eng} = \frac{PF_{eng}}{\int_{T_c}^{T_H} \kappa(T)\,dT} \quad \text{(S27)}$$

### d. Power density,

$$P_d = \frac{PF_{eng}\Delta T \quad m_{opt}}{L \quad (1+m_{opt})^2}; \qquad \text{(S28)}$$

$$m_{opt} = \sqrt{1 + (ZT)_{eng}\left({}^{\alpha}/_{\eta_c} - {}^{1}/_{2}\right)}$$

**e. Maximum TE efficiency,**

$$\eta_{max} = \frac{\eta_c \sqrt{1 + (ZT)_{eng}\left(\frac{\alpha}{\eta_c} - \frac{1}{2}\right)} - 1}{\sqrt[\alpha]{1 + (ZT)_{eng}\left(\frac{\alpha}{\eta_c} - \frac{1}{2}\right)} - \eta_c} \qquad \text{(S29)}$$

$$\eta_c = \frac{\Delta T}{T_H}; \qquad \alpha = \frac{S(T_H)\Delta T}{\int_{T_c}^{T_H} S(T)dT}$$

where ρ(T), S(T), $\eta_C$, α, and κ(T) stand for the temperature-dependent resistivity, Seebeck coefficient, Carnot efficiency, Thomson coefficient, and total thermal conductivity, respectively, and mopt refers to the ratio of the external load resistance (RL) to the internal resistance ($R_{int}$).

**3. The calculation for thermoelectric figure of merit and efficiency: (single-leg and uni-couple):**

**Uni-Couple**: In addition to zT and efficiency of single-leg TEG, we have also calculated the the average device figure of merit, $(ZT)_m$ for a uni-couple (*n*-type InSb and *p*-type ZnSb), where the hot and cold side temperatures were kept at 700 K and 300 K, respectively, using the expression given below,

$$(ZT)_{avg} = \int_{T_c}^{T_h} \frac{(S_p - S_n)^2 .\ T}{[\sqrt{\rho_p .\ \kappa_p} + \sqrt{\rho_n .\ \kappa_n}]^2 .\ \Delta T} dT \qquad \text{(S30)}$$

Where ($S_p$ and $S_n$), ($\rho_p$ and $\rho_n$) and ($\kappa_p$ and $\kappa_n$) represent Seebeck coefficient, electrical resistivity and total thermal conductivity of *p*-and *n*-type materials, respectively.

Using the $(ZT)_m$ value, the TE conversion efficiency of the above-mentioned pair of materials was theoretically calculated using the following equation,

$$\eta_{TE} = (\Delta T/T_h)\frac{\left(\sqrt{1+(ZT)_{avg}}-1\right)}{\left(\sqrt{1+(ZT)_{avg}}+\frac{T_c}{T_h}\right)} \quad \text{(S31)}$$

Where $\Delta T/T_h$ refers to the Carnot efficiency, $T_h$ and $T_c$ are the hot and cold side temperatures, and $(ZT)_{avg}$ is an average figure-of-merit of a pair of thermoelectric materials.

Table S1. Summarises the density ($\rho$), lattice parameters ($a = b = c$) and cell volume ($V$) of $InSb_{1-x}$ samples.

| ***Composition*** | ***ρ*** ***(g/cm³)*** | ***a =b = c*** **(Å)** | ***Cell volume*** **(Å)³** |
|---|---|---|---|
| InSb | 5.20 | 6.4795 | 272.04 |
| $InSb_{0.99}$ | 5.50 | 6.4794 | 271.99 |
| $InSb_{0.98}$ | 5.36 | 6.4791 | 271.97 |
| $InSb_{0.97}$ | 5.59 | 6.4789 | 271.96 |
| $InSb_{0.94}$ | 5.76 | 6.4783 | 271.88 |
| $InSb_{0.91}$ | 5.54 | 6.4782 | 271.76 |

Table S2. Presents the room-temperature carrier density ($n$), effective mass ($m^*$), electrical conductivity ($\sigma$), Seebeck coefficient (S) and thermal conductivity ($\boldsymbol{\kappa}$) and zT (at 623 K) of $InSb_{1-x}$ (x = 0.0, 0.02, 0.03, 0.06 and 0.09) samples.

| **Composition** | $n_e$ **. x $10^{16}$** **($cm^{-3}$)** **at 300 K** | ***m* ($m_e$)*** **at 300 K** | $\sigma$ **(S/m)** **at 300 K** | **S** **(μV/K)** **at 300 K** | **κ** **(W/mK)** **at 300 K** | **zT** **at 623 K** |
|---|---|---|---|---|---|---|
| InSb | -2.10 | 0.0162 | 3740 | -236 | 8.82 | 0.22 |
| $InSb_{0.98}$ | -3.60 | 0.0222 | 12357 | -254 | 7.06 | 0.8 |

| | | | | | | |
|---|---|---|---|---|---|---|
| $InSb_{0.97}$ | -3.71 | 0.0220 | 9380 | -246 | 9.24 | 0.44 |
| $InSb_{0.94}$ | -3.90 | 0.0329 | 19203 | -227 | 12.42 | 0.42 |
| $InSb_{0.91}$ | -4.26 | 0.0196 | 10721 | -229 | 10.23 | 0.35 |

**References:**


1 W. Kohn and L. J. Sham, *Physical Review*, 1965, **140**, A1133.

2 G. Kresse and J. Furthmüller, *Phys Rev B*, 1996, **54**, 11169.

3 G. Kresse and D. Joubert, *Phys Rev B*, 1999, **59**, 1758.

4 J. P. Perdew, A. Ruzsinszky, G. I. Csonka, O. A. Vydrov, G. E. Scuseria, L. A. Constantin, X. Zhou and K. Burke, *Phys Rev Lett*, 2008, **100**, 136406.

5 R. Nelson, C. Ertural, J. George, V. L. Deringer, G. Hautier and R. Dronskowski, *J Comput Chem*, 2020, **41**, 1931–1940.

6 A. Togo and I. Tanaka, *Scr Mater*, 2015, **108**, 1–5.

7 G. J. Snyder, A. H. Snyder, M. Wood, R. Gurunathan, B. H. Snyder and C. Niu, *Advanced Materials*, DOI:10.1002/adma.202001537.

8 J. Callaway, *Physical Review*, 1959, **113**, 1046.

9 J. Palraj, M. Sajjad, M. Moorthy, M. Saminathan, B. Srinivasan, N. Singh, R. Parasuraman, S. P. Patole, K. Mangalampalli and S. Perumal, *J Mater Chem A Mater*, 2024, **12**, 13860–13875.

10 M. Moorthy, P. Govindaraj, R. Parasuraman, A. Bhui, S. S. S. Gadhavajhala, B. Srinivasan, K. Venugopal and S. Perumal, *ACS Appl Energy Mater*, 2024, **7**, 2008–2020.

11 X. Cai and J. Wei, *J Appl Phys*, DOI:10.1063/1.4819224/367947.

12 M. Hong, Z. G. Chen, L. Yang, T. C. Chasapis, S. D. Kang, Y. Zou, G. J. Auchterlonie, M. G. Kanatzidis, G. J. Snyder and J. Zou, *J Mater Chem A Mater*, 2017, **5**, 10713–10721.

13 H. S. Kim, W. Liu, G. Chen, C. W. Chu and Z. Ren, *pnas.orgHS Kim, W Liu, G Chen, CW Chu, Z RenProceedings of the National Academy of Sciences, 2015•pnas.org*, 2015, **112**, 8205–8210.